

1 **Toward Improved Physics-Based Simulations of the LEO**
2 **Space Environment using GNSS-Enabled Small Satellites**

3 **Eric K. Sutton¹, Jeffrey P. Thayer^{1,2}, Marcin D. Pilinski³, Shaylah M. Mutschler²,**
4 **Thomas E. Berger¹, Vu Nguyen⁴, Dallas Masters⁴**

5 ¹Space Weather Technology, Research and Education Center (SWx TREC), University of
6 Colorado at Boulder.

7 ²Ann and H.J. Smead Aerospace Engineering Sciences, University of Colorado at Boulder.

8 ³Laboratory for Atmospheric and Space Physics (LASP), University of Colorado at Boulder.

9 ⁴Spire Global, Inc., Boulder, CO.

10 Corresponding author: Eric Sutton (eric.sutton@colorado.edu)

11 **Key Points:**

- 12 • GNSS-enabled satellites are capable of monitoring the state of the thermosphere at much
13 higher cadences than current operational datasets
- 14 • We present an initial technique to infer neutral densities from orbit determination
15 products of the Spire CubeSat constellation
- 16 • Densities are used to drive a data-assimilative, physics-based model of the thermosphere
17 and ionosphere during 23 Sept.–9 Dec. 2018

18 **Abstract**

19 Satellite-atmosphere interactions cause large uncertainties in low-Earth orbit determination and
20 prediction. Thus, knowledge of and the ability to predict the space environment, most notably
21 thermospheric mass density, are essential for operating satellites in this domain. Recent progress
22 has been made toward supplanting the existing empirical, operational methods with physics-
23 based data-assimilative models by accounting for the complex relationship between external
24 drivers and their response in the upper atmosphere. Simultaneously, a new era of CubeSat
25 constellations is set to provide data with which to calibrate our upper-atmosphere models at
26 higher resolution and cadence. With this in mind, we provide an initial method for converting
27 precision orbit determination (POD) solutions from global navigation satellite system (GNSS)
28 enabled CubeSats into timeseries of thermospheric mass density. This information is then fused
29 with a physics-based, data-assimilative technique to provide calibrated global densities.

30 **1 Introduction**

31 Within low-Earth orbit (LEO), a region spanning roughly 100 to 1000 km in altitude for
32 the purposes of this paper, interactions between man-made satellites and the ambient atmosphere
33 cause large uncertainties in the orbit determination and prediction processes (Berger et al., 2020).
34 During episodic periods of moderate to severe space weather activity, such atmospheric drag
35 uncertainties can amplify by a factor of 2–5 in a matter of minutes to hours (Krauss et al., 2015;
36 Sutton et al., 2005). These uncertainties, when combined with the steadily growing launch rate of
37 small satellites and CubeSats and our advancing ability to track smaller and smaller objects, are
38 poised to overwhelm the U.S. Department of Defense infrastructure currently carrying out the
39 Detect–Track–Catalog mission. Products of this mission are pervasive across the Space
40 Situational Awareness (SSA) and Space Traffic Management (STM) enterprises and form a
41 critical infrastructure for nearly all space-based activities. Thus, knowledge and prediction of the
42 space environment, particularly the neutral mass density of the thermosphere and lower
43 exosphere, are an essential part of satellite operations within LEO.

44 One of the major obstacles in predicting orbit trajectories hours to days in advance, and in
45 correlating consecutive or irregular object tracks, comes from the legacy framework used to
46 model the upper atmosphere’s state and its interaction with satellites and debris. The current
47 model employed by the Combined Space Operations Center (CSpOC) and is the High Accuracy

48 Satellite Drag Model (HASDM) (Storz et al., 2005), an empirical model that self-calibrates by
49 ingesting ground-based tracking data of a select set of orbiting “calibration objects”—i.e.,
50 operational and defunct satellites passing through LEO with reasonably stable ballistic
51 coefficients. While this method provides an accurate global-average snapshot of the upper
52 atmosphere, its abilities to capture realistic spatial structure and forecast into the future are
53 limited. Physics-based upper atmosphere simulation approaches offer a vast potential
54 improvement in this regard. Models in this category solve a set of Navier-Stokes fluid equations
55 that have been appropriately tailored for use in the upper atmosphere and are therefore inherently
56 better equipped for simulating a dynamic system response to impulsive energy input from the
57 solar wind. For years the computational cost of these models prohibited their use in an
58 operational setting. However, present-day computing technology is abundantly capable of
59 running an ensemble of such models in near real time. Instead, the primary reason that physics-
60 based methods remain to be adopted by operational centers is the lack of robust data assimilation
61 schemes capable of self-calibrating at levels equal to or better than those currently used in
62 combination with empirical models.

63 Fortunately, significant strides have been made in recent years toward supplanting
64 empirical methods with physics-based data assimilative models of the upper atmosphere. One
65 such advancement has been accomplished by accounting for the complex relationship between
66 external drivers—namely solar flux and geomagnetic heating—and the response of the upper
67 atmosphere by employing a new least-squares filter called the Iterative Driver Estimation and
68 Assimilation (IDEA) technique (Sutton, 2018). The new filter operates similarly to an unscented
69 Kalman filter (UKF) with the addition of mechanisms to accommodate the lagged response of
70 the upper atmosphere to variations in the external drivers. Using this new technique, notable
71 improvements in spatial accuracy—even during a geomagnetic storm—have already been
72 demonstrated (Sutton, 2018), which can help to lower uncertainty across the LEO catalog and
73 increase the efficiency of Space Traffic Management (STM) activities. In addition, the
74 emergence of large constellations of commercial and academic CubeSats over the past 5 years
75 brings with it an excellent opportunity. Most newer SmallSats and CubeSats are equipped with
76 Global Navigation Satellite System (GNSS) devices, making them valuable sources of Precision
77 Orbit Determination (POD) information. Many are also equipped with the ability to monitor their

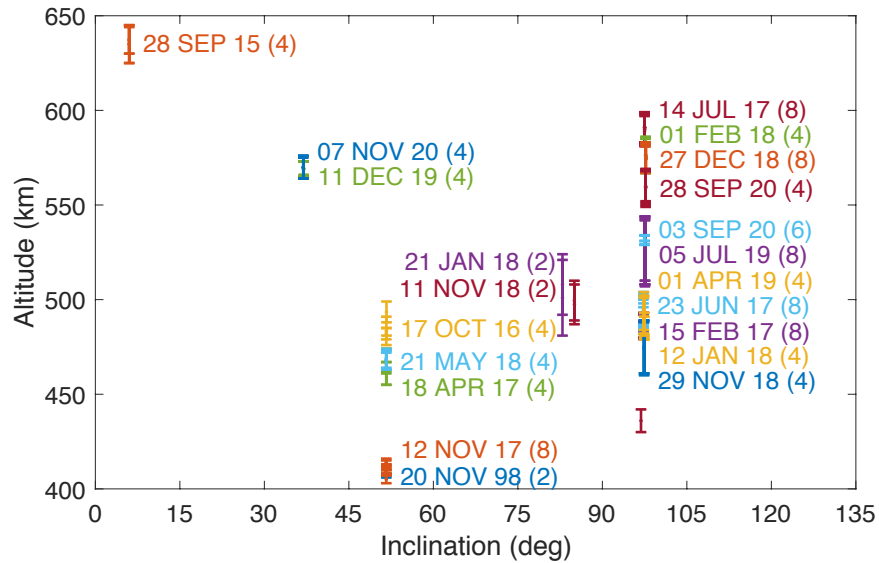
78 attitude, allowing the construction of an accurate force model. This information can be combined
79 to initialize and constrain models of the upper atmosphere.

80 In order to track the state of the upper atmosphere with reasonable fidelity, the HASDM
81 model ingests observations from ground-based radar tracks of known objects using a similar
82 technique to the one we present here. However, in order to make strides in specifying and
83 predicting the state of the thermosphere, new data sets with increased resolution, cadence, and
84 coverage are needed (Bruinsma et al., 2021). Satellite-based GNSS observations are capable of
85 describing the space environment at a much higher spatial resolution and temporal cadence.
86 Whereas the conventional radar-derived, satellite-drag data sets operate on a multi-orbit to multi-
87 day cadence, we will show that the GNSS-derived data sets are capable of operating at a cadence
88 of a single orbit. Even higher cadences may also be possible but will require further
89 development. The remainder of the paper details our efforts to use the new set of information
90 provided by CubeSats to drive a physics-based, data-assimilative approach to simulating
91 atmospheric densities in LEO.

92 **2 Datasets**

93 Spire operates a constellation of over 100 CubeSats in LEO with altitudes ranging from
94 400–650 km and inclinations spanning the globe, from equatorial to polar orbits. Figure 1 gives a
95 snapshot of the distribution of altitude and orbit inclination of Spire CubeSats as of late January
96 2021.

97



98

99 **Figure 1.** Current coverage of altitude versus inclination for the Spire constellation of CubeSats
 100 (as of 26 January 2021). The error bars show the perigee-to-apogee range of altitudes. CubeSats
 101 are color coded by common launch dates with the total number of CubeSats in each launch group
 102 indicated in parentheses.

103 The data sets used in this study were provided by Spire Global as part of the NASA
 104 Commercial SmallSat Data Pilot Program and cover the period of 23 Sept.–9 Dec. 2018. For the
 105 purposes of our work, the following data products were utilized:

- 106 • Precision Orbit Determination (POD) solution ephemeris derived from GNSS tracking
- 107 • Satellite pointing in the form of attitude quaternions
- 108 • Satellite geometry model

109 POD solutions were typically available during the duty cycle of the GNSS/Radio
 110 Occultation (RO) instrument. For the 2018 dataset, duty cycles were in the range of 30–40% of
 111 the time, usually concentrated along 40- to 60-minute segments of an orbit (referred to hereafter
 112 as an orbit arc). This efficiency has increased with more recent CubeSat builds such that current
 113 duty cycles are beginning to approach 100%. For the current data set, ephemeris from each orbit
 114 arc were estimated using the RTOrb software ([https://gps-
 115 solutions.com/brochures/GPSS_Brochure_RTOrb_Nov_2011.pdf](https://gps-solutions.com/brochures/GPSS_Brochure_RTOrb_Nov_2011.pdf)). This software implements a
 116 Kalman filter-based approach to estimate orbit ephemeris. As configured for the current dataset,
 117 RTOrb considers Earth's gravity up to degree and order 120 from the EIGEN-2 model (Reigber

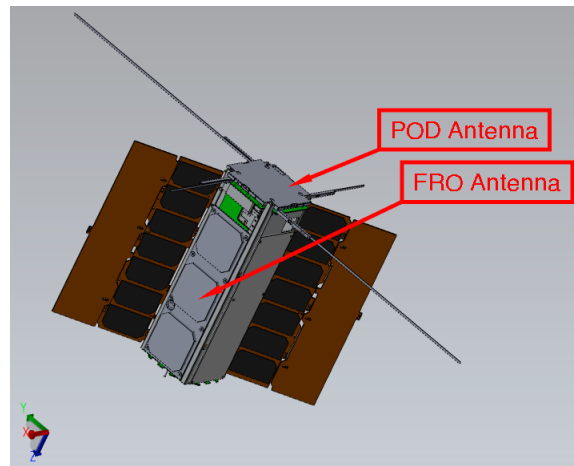
118 et al., 2003), Luni-Solar 3rd body perturbations, atmospheric drag assuming densities from the
119 Mass Spectrometer Incoherent Scatter extension (MSISE-90) model (Hedin, 1991), and solar
120 radiation pressure (SRP) with cylindrical Earth-shadowing effects. The latter two effects use a
121 cannonball approach in which coefficients of drag and reflectivity are estimated within each arc,
122 respectively, along with the orbit ephemeris. The treatment of drag and SRP in the POD process
123 is not to be confused with the force model described later in this section; instead, the parameters
124 estimated here have little bearing on our calculations of orbit energy.

125 The attitude of the Spire CubeSats is represented by a quaternion describing the
126 transformation from the body-fixed coordinate system (see Figure 4 below) to the vehicle
127 velocity/local horizontal (VVLH) orbit-based coordinate system at a given instance in time.
128 These data enable the orientation of the satellite with respect to the final coordinate system
129 introduced in Section 3.2. In the initial phases of the NASA Data Pilot assessment, quaternions
130 were provided at an approximate cadence of 10 seconds during the duty cycle of the GNSS/RO
131 receiver, with nothing available outside of the duty cycle. However, it was realized early on in
132 the project that, due to frequent orientation maneuvers, the accuracy of the retrieved neutral
133 densities would be limited by any breaks in continuity of satellite attitude data (see Section 3.3
134 for further details). The attitude mode of the CubeSats frequently switched between an observing
135 mode aligning GNSS/RO antennas along track and a mode that maximizes the amount of solar
136 flux incident on the solar panels. Because these changes in orientation modify the integrated
137 effect that atmospheric drag has on the orbit parameters, the orientation must be monitored
138 constantly in order to convert orbital energy loss rates to an atmospheric density. Spire has since
139 updated their processing chain for the entire fleet to ensure that a continuous stream of attitude
140 quaternions is available for any datasets originating after 2018. However, for the 2018 data set,
141 processing was limited to a small subset of three CubeSats from Spire Global's constellation for
142 which attitude data had been continuously downlinked and archived. These satellites, which will
143 be used throughout the remainder of the paper, are referred to by Spire's internal satellite ID
144 numbers: 83, 84, and 85. These three CubeSats trace back to a common launch on 21 May 2018
145 into a 51.6° inclination orbit. During the time period of interest these satellites orbited between
146 the altitudes of 467–492 km. Additional properties and designations of these CubeSats can be
147 found in Table 1.

148 **Table 1.** Properties of Spire CubeSats used in this study

Spire ID	NORAD ID	COSPAR ID	Perigee/Apogee Altitude (km)	Inclination (degrees)	S/C Mass (g)
83	43560	2018-046G			
84	43559	2018-046F	467–492	51.6	4933 ± 4
85	43558	2018-046E			

149 Figure 2 shows the geometry for the three Spire CubeSats. The GNSS/POD antenna
 150 nominally points in the zenith direction while the front radio occultation (FRO) antenna
 151 generally points along the in-track or anti-in-track directions when the satellite is recording RO
 152 data. When the RO instrument is cycled off, the satellite reorients in such a way as to maximize
 153 illumination of the solar panels.



154

155 **Figure 2.** Computer model of Spire's version 3.3 Lemur CubeSat.156 **3 Methods**157 **3.1 Orbital Energy Determination**

158 To drive our data assimilative process, we use information from GNSS measurements
 159 taken aboard CubeSats. There are several methods available to infer neutral densities from orbit
 160 positioning information. For instance, this can be done by estimating a scaling correction for a
 161 density model within a POD solution using two-line element (TLE, e.g., Brandt et al., 2020) sets
 162 or GNSS tracking (e.g., van den IJssel & Visser, 2007) . We choose instead to employ a model-
 163 agnostic energy tracking method that uses the existing POD solutions routinely obtained by

164 Spire. The first step is to calculate the orbital energy at each available ephemeris data point and
 165 track the change in this quantity between subsequent orbits. For an Earth-orbiting satellite, this
 166 energy can be approximated in the following way:

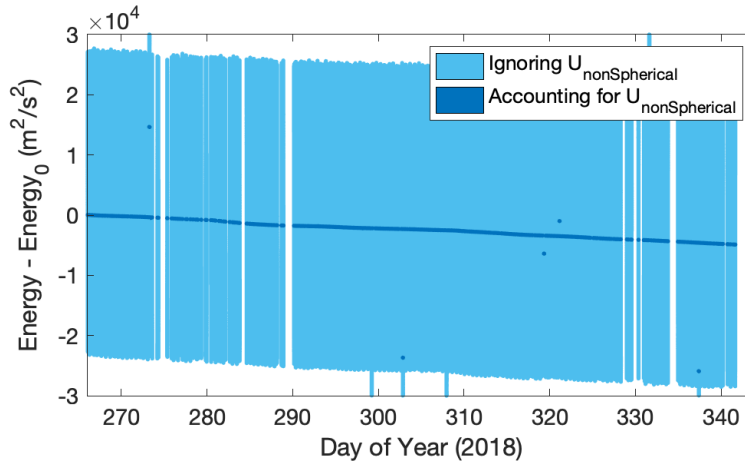
$$167 \quad \xi = \frac{v^2}{2} - \omega_{Earth}^2 \frac{x^2 + y^2}{2} - \frac{\mu}{r} + U_{nonSpherical} \quad (1)$$

168 where $r = \sqrt{x^2 + y^2 + z^2}$ and v are the satellite's respective position and velocity in an
 169 Earth-centered Earth-fixed (ECEF) coordinate frame, ω_{Earth}^2 is the rotation rate of the Earth, μ is
 170 the gravitational parameter for the Earth, and $U_{nonSpherical}$ is a potential function composed of
 171 the non-spherical terms of Earth's gravity. In the absence of nonconservative forces (e.g.,
 172 atmospheric drag or solar radiation pressure) or any additional perturbing conservative forces
 173 (e.g., 3rd body attraction, solid Earth tides, ocean tides, atmospheric tides, etc.), ξ is a conserved
 174 quantity along the orbit of a satellite.

175 We have found that the choice of Earth-fixed coordinates becomes important when
 176 considering non-spherical gravity terms in the energy equation (Equation 1), particularly any
 177 non-zonal terms (i.e., order $m > 0$). In ECEF coordinates, $U_{nonSpherical}$ is clearly a function of
 178 position alone. The alternate formulation of the energy equation in an inertial coordinate frame,
 179 however, would require $U_{nonSpherical}$ to be a function of both position and time, violating the
 180 assumptions underlying a potential function and its use in the energy equation. As a result, the
 181 formulation of energy in an inertial coordinate frame does not remain constant along an orbit
 182 when considering non-zonal terms—even in the absence of nonconservative forces—and leads to
 183 twice-daily oscillations of approximately ± 130 – 140 J/kg/s or m^2/s^3 for the orbits analyzed in
 184 this paper, or equivalently, about ± 30 – 35 m in the semi-major axis. Much of this can be directly
 185 attributed to the $n = m = 2$ gravitational potential term, which is the largest non-zonal term in
 186 $U_{nonSpherical}$.

187 If we describe the Earth's gravity field using the two-body approximation—ignoring for a
 188 moment the non-spherical contribution—the energy dissipation due to atmospheric drag remains
 189 obscured by the large variations in energy due to the J2 and higher-order gravitational terms. The
 190 light blue data points in Figure 3 show this simplified calculation of orbital energy for a single
 191 CubeSat from Spire Global's constellation (satellite 83) during the period spanning 23 Sept.–9
 192 Dec. 2018. However, when we account for a 36x36 spherical harmonic gravity field as depicted

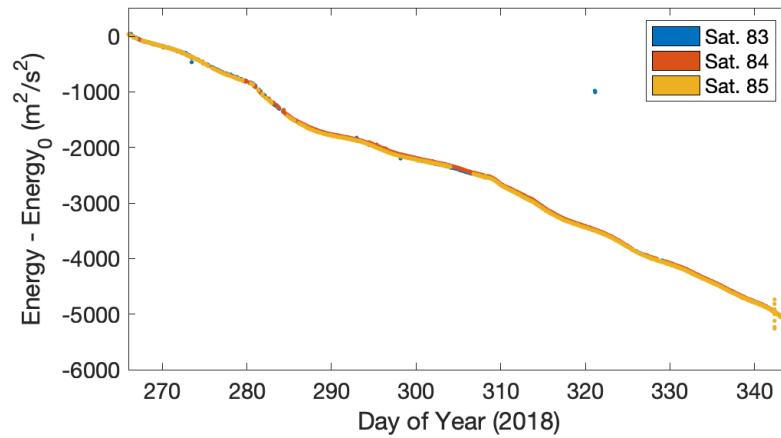
193 by the dark blue curve, the change in energy caused by atmospheric drag is more readily isolated
 194 from variations in the gravity field.



195

196 **Figure 3.** Keplerian orbital energy (light blue curve, i.e., ignoring the $U_{nonSpherical}$ term from
 197 Equation 1) and total orbital energy (dark blue curve, i.e., including the $U_{nonSpherical}$ term from
 198 Equation 1) for Spire CubeSat 83 during the period of 23 Sept.–9 Dec. 2018.

199 Figure 4 depicts the orbital energy of all three CubeSats over the same time span as
 200 Figure 3 but zoomed in to reveal variations in the rate of decay. To conform with the POD
 201 solutions, we have used the non-spherical terms specified by the EIGEN-2 gravity model
 202 (Reigber et al., 2003). We found that, for our purposes, including terms above a 36x36 expansion
 203 yielded diminishing returns.



204

205 **Figure 4.** Orbital energy (i.e., including the $U_{nonSpherical}$ term from Equation 1) for Spire
 206 CubeSats 83, 84, and 85 during the period of 23 Sept.–9 Dec. 2018.

207 During this period of time, the energy curves track one another quite well due, in part, to
 208 the fact that all three CubeSats occupy essentially the same orbital plane. Changes in energy
 209 were on the order of $5000 \text{ m}^2/\text{s}^2$ over the entire period of analysis, or about $65 \text{ m}^2/\text{s}^2$ per day.
 210 This is equivalent to a change in the semi-major axis of 1.2 km total, or about 15 meters per day.
 211 These magnitudes are specific to the size, shape and ballistic coefficients of the satellites, as well
 212 as the altitude and prevailing geophysical conditions sampled during the time period of interest.
 213 After applying a simple filter to reject erroneous arcs (note the obvious outliers on day 273, 320,
 214 and 342 in Figure 4), the noise level of these timeseries of orbital energy becomes low enough to
 215 derive an effective energy dissipation rate between subsequent orbit arcs.

216 3.2 Satellite Force Model

217 To interpret the timeseries of energy from Figure 4 in terms of the behavior of the upper
 218 atmosphere, it is necessary to understand how the satellite drag interaction depends on
 219 atmospheric density. The rate at which energy is lost from a satellite's orbit to the atmosphere
 220 via the drag force, or the energy dissipation rate (EDR), can be related to atmospheric mass
 221 density through the following equation:

$$222 \quad EDR \equiv -\frac{d\xi}{dt} = \frac{1}{2m} C_D A_{ref} \rho v^3 \quad (2)$$

223 where C_D is the satellite's coefficient of drag, A_{ref} is the cross-sectional area of the
 224 satellite projected in the direction of v , the velocity of the satellite in the ECEF coordinate frame,

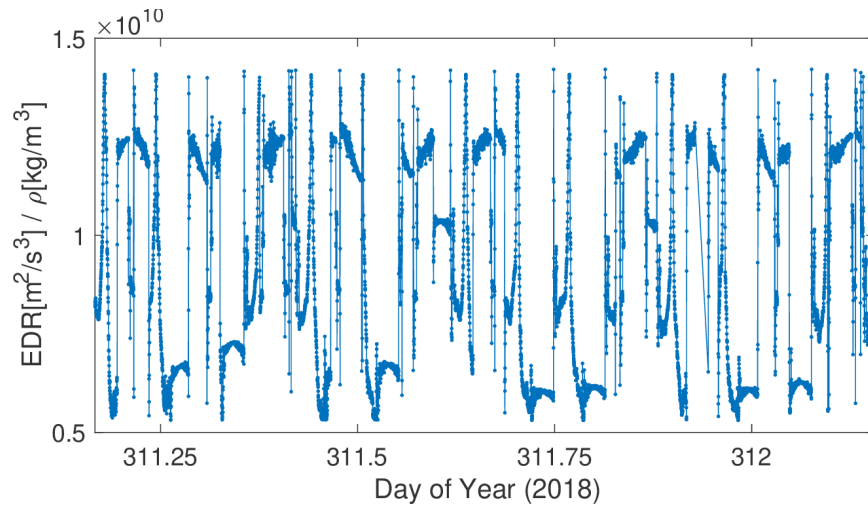
225 m is the satellite mass, ρ is the mass density. Winds are neglected in this equation, however, the
 226 co-rotation of the atmosphere with the Earth is automatically considered through the use of
 227 ECEF coordinates. To compute the coefficient of drag, we consider the transfer of momentum
 228 between incoming atmospheric particles and the satellite surface assuming that particles are
 229 accommodated to the approximate surface temperature of the satellite using an accommodation
 230 coefficient of $\alpha = 0.93$ (Sutton, 2009). While the accommodation coefficient is kept constant,
 231 both C_D and A_{ref} can vary significantly over the course of an orbit due to changes in the attitude
 232 of the satellite.

233 In order to compare two subsequent observations of orbital energy ξ_0 and ξ_1 calculated
 234 by Equation 1 at their respective epochs t_0 and t_1 , Equation 2 can be integrated to find the
 235 dependence on atmospheric density:

$$236 \quad \xi_1 - \xi_0 = -\frac{1}{2m} \int_{t_0}^{t_1} C_D A_{ref} \rho v^3 dt = -\frac{1}{2m} \rho_{eff} \int_{t_0}^{t_1} C_D A_{ref} v^3 dt \quad (3)$$

237 Solving for ρ_{eff} , similar in theme to the work of Picone (2005), gives an effective mass
 238 density between t_0 and t_1 along the orbit of the satellite.

239 Figure 5 shows the simulated change in orbital energy normalized by neutral density
 240 (EDR/ρ) as given by Equation 2 for one of Spire Global's CubeSats according to its orientation
 241 over the course of a single day. This parameter, which we can refer to simply as the force model,
 242 is the conversion factor between the observed energy dissipation rate and atmospheric density.
 243 The periodic shift between pointing modes—one optimized for RO sensing and the other for
 244 solar panel illumination—can be clearly seen in Figure 5. Accounting for the large variations in
 245 the force model becomes crucial because a satellite can dwell in a given pointing mode for a
 246 significant fraction of an orbit, and this dwell time is not necessarily consistent between orbits. If
 247 neglected, these approximate factor-of-two variations in the force model have the potential of
 248 causing errors of similar magnitude in the density retrievals.



249

250 **Figure 5.** Force model for Spire CubeSat 83 for a single day starting early on 7 Nov. The force
 251 model is the conversion factor between the observed energy dissipation rate and atmospheric
 252 density.

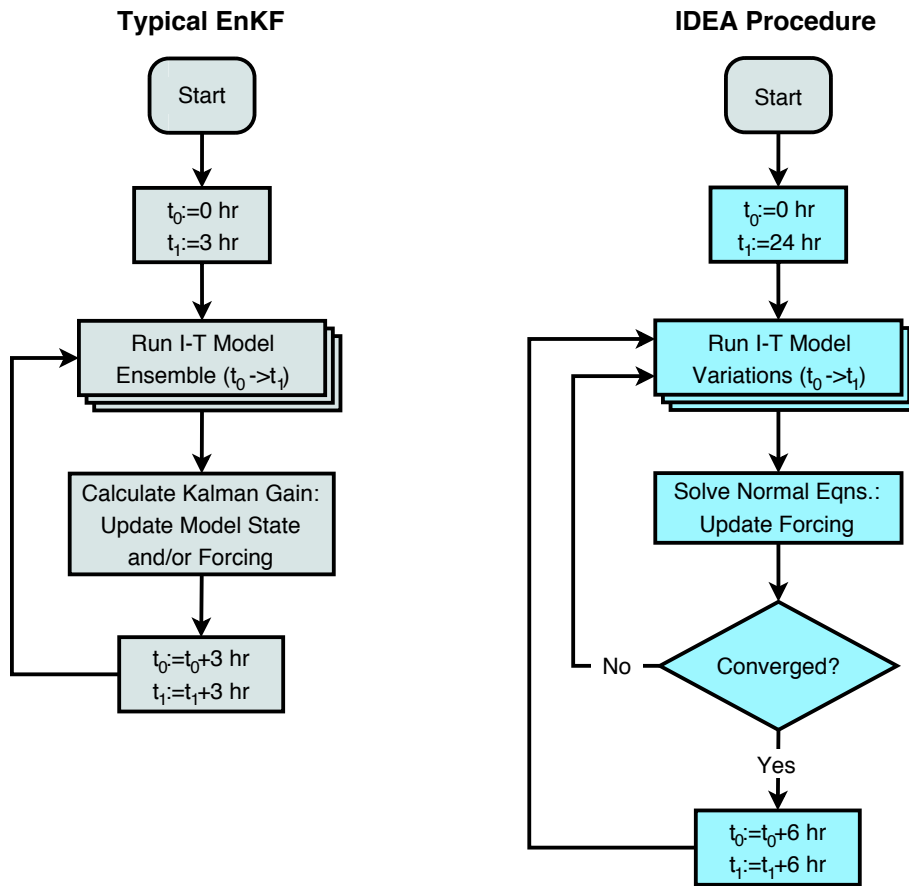
253 3.3 Data Assimilation

254 After processing the GNSS measurements and applying the force model described above,
 255 the final step in our process is to ingest these observations into a data assimilative framework to
 256 correct the global upper atmospheric density. Here we briefly describe the Iterative Driver
 257 Estimation and Assimilation (IDEA) technique, based on the method of Sutton (2018). This
 258 method accounts for the complex relationship between external drivers—namely solar flux and
 259 geomagnetic heating—and the resulting response of the upper atmosphere. In general, these
 260 drivers are poorly monitored and often rely on proxies that only very approximately represent the
 261 physical mechanisms heating and energizing the upper atmosphere. To represent the absorption
 262 of solar extreme and far ultraviolet (EUV/FUV) irradiance, the solar radio flux at 10.7 cm
 263 wavelength (F10.7) is often used as a proxy. In terms of the solar wind–magnetosphere–
 264 ionosphere–thermosphere interaction, the geomagnetic Kp index is often used to characterize
 265 heating and momentum exchange at high latitudes. Parameterized coupling functions are then
 266 used to convert these proxies into atmospheric heating, incurring further uncertainty into the
 267 overall modeling process. The reliance on these proxies and their coupling functions leads to
 268 large uncertainties when driving a model of the thermosphere.

269 IDEA estimates corrections to the external forcing parameters and their coupling
270 functions in order to bring a physics-based model into better agreement with direct observations
271 of the thermosphere. The discrepancies between model output and observations are minimized
272 by employing a least-squares filter similar in nature to an unscented Kalman filter (UKF). Figure
273 6 compares the IDEA process (right) to that of a typical ensemble Kalman filter (EnKF)
274 configured for ionosphere/thermosphere modeling. IDEA runs several versions of the
275 thermosphere model, each experiencing slightly different external driving conditions.

276 In the current implementation of IDEA, the Thermosphere–Ionosphere–Electrodynamics
277 General Circulation Model (TIEGCM) (Qian et al., 2014; Richmond et al., 1992; Sutton et al.,
278 2015) is used as the physics-based environment model. TIEGCM is a finite-difference solution to
279 the conservation equations of momentum, mass, and energy describing the upper atmosphere in
280 the presence of momentum and energy sources. TIEGCM accounts for the dominant features in
281 the upper atmosphere of molecular diffusion and circulation, solar heating in the EUV and FUV
282 bands, and high-latitude auroral heating. TIEGCM also has the ability to simulate the ionosphere
283 and associated electrodynamic coupling between the neutral and plasma environment in a self-
284 consistent manner at middle and low latitudes.

285 In terms of data assimilation, additional measures must be taken to deal with the lagged
286 response of the upper atmosphere to variations in the external drivers. It is well known that the
287 response of the thermosphere can take on a large range of timescales depending on several
288 factors, height being among the largest contributors. In order for an estimated correction of the
289 external forcing parameters to have a timely effect on the model, the time-lagged response must
290 be accounted for. IDEA abandons the sequential filtering techniques typically used for
291 ionosphere/thermosphere applications (e.g., M. V. Codrescu et al., 2004, 2021; S. M. Codrescu
292 et al., 2018; Fuller-Rowell et al., 2004; Godinez et al., 2015; Matsuo et al., 2012, 2013; Minter et
293 al., 2004; Morozov et al., 2013; Murray et al., 2015). Instead, an iterative approach is adopted so
294 that estimated forcing parameters can be re-applied to a simulation over the course of a day so
295 that the model can respond to forcing (refer to the additional feedback loop on the right side of
296 Figure 6).



297

298 **Figure 6.** Comparison of a typical Ensemble Kalman Filter as configured for use with a time-
 299 dependent thermospheric model (left) with the IDEA technique (right; features in color differ
 300 from their counterparts in the EnKF flow chart on the left), where t_0 and t_1 are the respective start
 301 and end times of the model runs during a given data assimilation cycle (adapted from Sutton,
 302 2018).

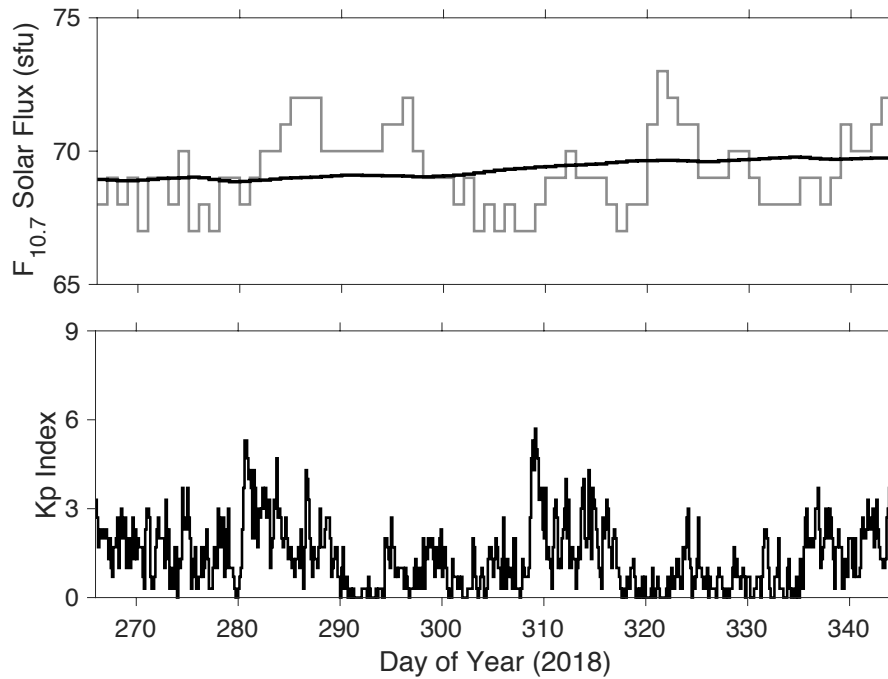
303 In Sutton (2018), satellite-borne accelerometer observations of thermosphere density
 304 were used to calibrate the external forcing parameters driving the TIEGCM. Here we use EDRs
 305 based on POD ephemeris derived from GNSS measurements from 3 satellites from Spire
 306 Global's constellation of CubeSats. A forward model, based on output from the TIEGCM, the
 307 satellite geometry model shown in Figure 2, and the force model of Sutton (2009), is used to
 308 synthesize orbital energy dissipation for each satellite according to Equation 3. Accelerometer
 309 data operates at high cadence (0.1–1 Hz) equating to a resolution of 7–70 km along the satellite's
 310 orbit. The GNSS/POD data set yields a measurement of density more on the order of once per
 311 orbit arc (possibly higher with additional development). This difference in information content

312 between data sets necessitates additional consideration when designing a thermospheric
313 estimation filter. In this case, we found that the observability of IDEA was limited to estimation
314 of the most recent daily $F_{10.7}$ value and the most recent 6-hourly effective Kp value. For
315 comparison, Sutton (2018) found it possible to estimate the most recent daily $F_{10.7}$ value and the
316 three most recent 3-hourly Kp values when using the high-resolution accelerometer-derived
317 density data set. However, it is expected that improvement in observability will be enabled
318 through the use of more CubeSats in the estimation process. And considering the greater
319 coverage of CubeSats in altitude and local time, accuracy could very easily exceed
320 accelerometer-based density model corrections.

321 **4 Results and Discussion**

322 The period spanning 23 Sept.–9 Dec. 2018 (days 266–343) of our study was marked with
323 very low activity in terms of the magnitude and variation of solar EUV and FUV, as
324 approximated by measurements of the 10.7 cm solar radio flux ($F_{10.7}$; top panel of Figure 7).
325 Note that $F_{10.7}$ has an approximate lower bound of 66 solar flux units (sfu) at solar minimum and
326 attains values above 200 during solar maximum. During the latter, 27-day solar rotational
327 modulation can also produce large swings in $F_{10.7}$ with concomitant signals in the thermospheric
328 density. Because the 2018 period falls firmly within solar minimum, the variations seen here are
329 quite small. In terms of geomagnetic activity, however, there were two minor-to-moderate
330 disturbances on 7 Oct. (day 280) and 4 Nov. (day 308) as shown by the 3-hourly Kp
331 geomagnetic index (lower panel of Figure 7).

332

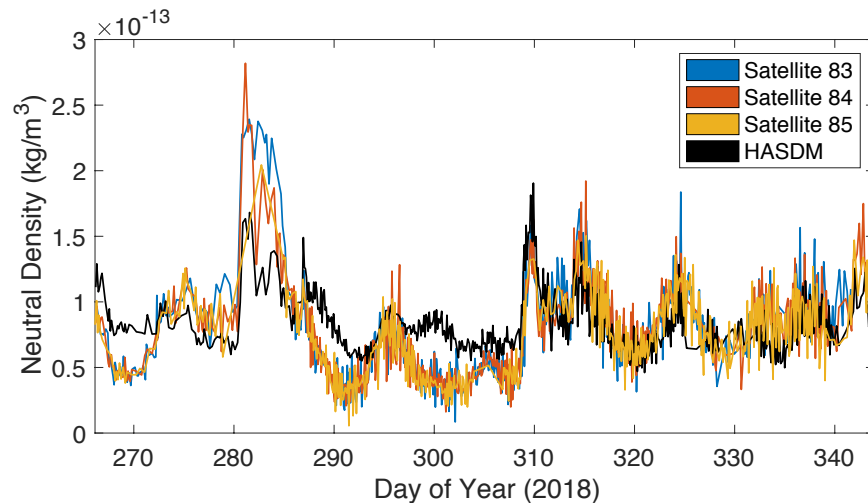


333

334

335 **Figure 7.** Top: observed solar $F_{10.7}$ radio flux. The grey curve is the daily measured value from
 336 the Ottawa observatory normalized to 1 AU sun-earth distance; the black curve is an 81-day (~ 3
 337 solar rotation) centered average. Bottom: the 3-hourly planetary magnetic index Kp. Both panels
 338 span the period of interest 23 Sept.–9 Dec. 2018.

339 Given observations of orbital variations and an appropriate force model as discussed in
 340 the previous section, an effective atmospheric mass density can be inferred between orbit arcs.
 341 Figure 8 shows such neutral mass densities derived from the three CubeSats (blue, red and
 342 yellow curves) of Spire’s constellation. The cadence of these densities is approximately one
 343 measurement per orbit arc. For the time period studied, this equates to a cadence of about 2–2.5
 344 hours on average. This cadence depends on the instrument duty cycle, which has steadily
 345 improved since 2018. A higher cadence may be possible in the future as duty cycle improves,
 346 however, the exact allowable cadence will also depend on the altitude of the satellite and the
 347 noise errors of the GNSS measurements. HASDM output is also shown with the black curve for
 348 reference. This empirical model is calibrated by ground-based radar tracking observations of
 349 approximately 70–90 orbiting objects. Because the individual tracking observations are sparse—
 350 relative to those available from GNSS—densities derived from this technique have an effective
 351 cadence of several hours to several days (Storz et al., 2005).



352

353 **Figure 8.** Neutral mass densities derived from Spire CubeSats 83–85. Also shown is output from
 354 HASDM as sampled on the orbit of satellite 84. The values plotted are the effective densities
 355 (see the right-hand side of Equation 3) between subsequent orbit arcs.

356 The CubeSat-derived densities maintain good agreement with one another and reasonable
 357 agreement with HASDM. As Figure 7 shows, there are several minor to moderate variations in
 358 K_p over the time interval. The signatures of these disturbances are also seen in the neutral
 359 densities of Figure 8. There are several deviations between data and model though, most notably
 360 around days 270, 290, and 300, where CubeSat-derived densities are significantly lower than
 361 HASDM. We have not yet concluded whether model or data are in error during these intervals,
 362 since very little ground-truth data exists during this period for validation. Another period of
 363 discrepancy exists around the geomagnetic disturbance on day 280, where CubeSat-derived
 364 densities experience a much larger storm-time increase. We note that POD data were less
 365 frequent during this particular event than during other times. Additionally, attitude data was
 366 unavailable for satellite 83 over much of the disturbance, particularly day 282–285. The
 367 discrepancy in amplitude during this event could also be a function of the higher cadence of the
 368 CubeSat POD data fit spans (5–6 hours during this event) relative to that of the HASDM data fit
 369 spans (~ 1 day or more), in which case, the CubeSat-derived densities would be expected to more
 370 accurately resolve the storm-time disturbance.

371 In general, some noise in the observations and modeled output is expected, with
 372 instrumental, data sampling, and geophysical origins. Part of this noise is caused by variations in
 373 sampling location for a given data point. In other words, the data points presented in Figure 8 do

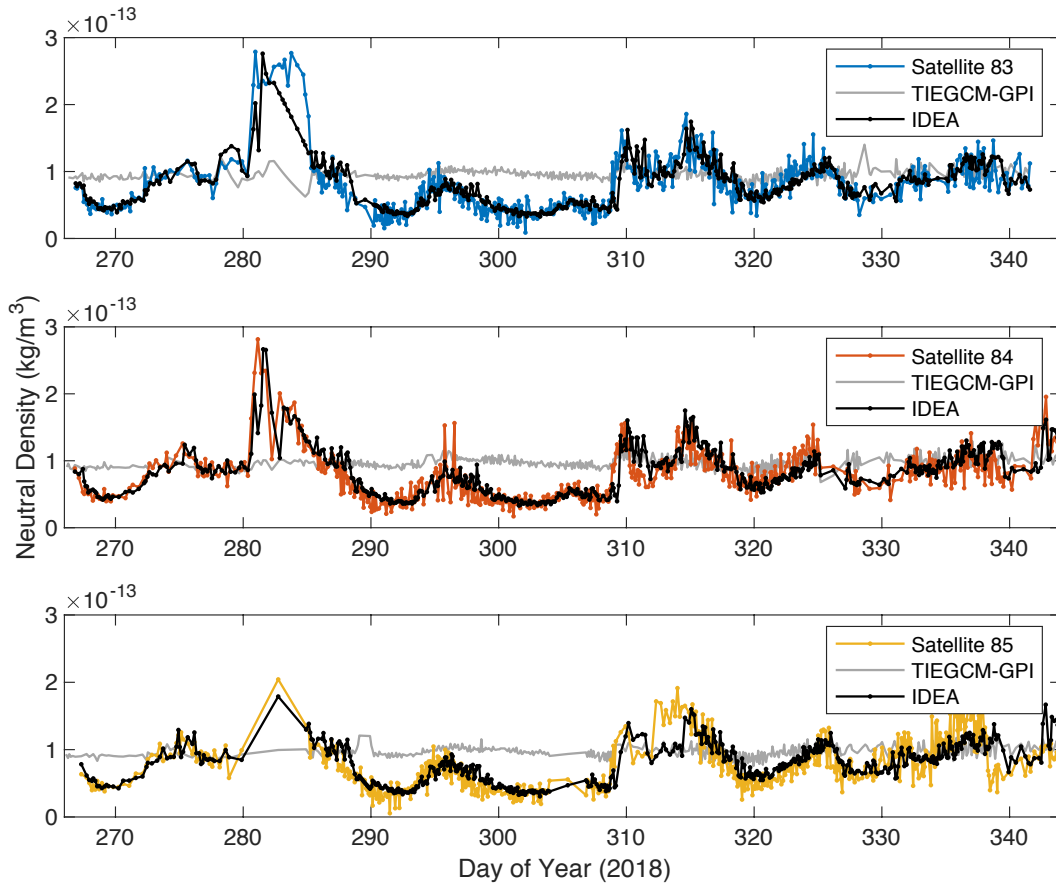
374 not represent the density averaged over a complete orbit; instead, each data point can be sampled
375 over a very different part of the globe than the previous. The resulting noise can be seen in the
376 HASDM model, which if plotted as an average over full orbits, would appear much more
377 smooth. Another important source of noise in the density timeseries comes directly from
378 uncertainties in the POD solutions themselves. Because the POD solutions were not designed
379 with a thermospheric application in mind, we expect that some of the estimation parameters may
380 have been overfit. And finally, there is certainly an amount of geophysical variability seen in the
381 observed density timeseries that is not captured in by the HASDM model. While an in-depth
382 error analysis is beyond the scope of the present work, we will continue to investigate techniques
383 to minimize this noise, including improving the underlying POD solutions and combining
384 timeseries from additional satellites.

385 A central goal of this work is to ingest multiple data sources into a physics-based,
386 assimilative thermosphere model to combine information and mitigate the uncertainty of any one
387 dataset. Figure 9 shows the baseline TIEGCM simulation without any assimilation (grey curve)
388 driven externally by the observed geophysical indices (GPI) of K_p and $F_{10.7}$; the POD-based
389 densities derived using the techniques described in the previous Section (blue, red, and yellow
390 curves); and the IDEA output over the interval spanning 23 Sept.–9 Dec. 2018 (solid black
391 curves).

392 The baseline TIEGCM-GPI simulation shows muted response to the K_p and $F_{10.7}$ inputs
393 during this solar-minimum interval, when compared with the IDEA output (or with the HASDM
394 output in Figure 8). CubeSat densities and IDEA output agree very well over the interval. There
395 are, however, several short periods when POD data from a single satellite becomes sparse, such
396 as the period around day 304–306 for satellite 85 (yellow curve), or when attitude data becomes
397 unavailable, such as the period around day 282–285 for satellite 83 (blue curve). There are also
398 several periods during which data from a single satellite becomes spurious, not agreeing with the
399 data from the other two satellites, such as the period around 335–340 for satellite 85 (yellow
400 curve). In these cases, the other two data sets tend to compensate for missing or spurious data
401 from the third satellite. This leads us to believe that adding data from additional satellites and
402 constellations should improve performance and increase the "signal-to-noise ratio" of the data
403 assimilation process.

404 The performance of these models with respect to the CubeSat-derived densities are
 405 assessed using the metrics of Sutton (2018). These consist of the mean (μ), standard deviation
 406 (σ), and root mean square error ($RMSe$) of the ratio of model density to observed density, all
 407 computed in logarithmic space:

$$408 \quad \mu(m/o) = \exp\left(\frac{1}{N} \sum_{i=1}^N \ln \frac{\rho_{m,i}}{\rho_{o,i}}\right) \quad (4)$$



409
 410 **Figure 9.** Comparison of observations with model output. CubeSat-derived densities are given
 411 by the colored curves for satellites 83 (top), 84 (middle), and 85 (bottom). Also shown is the
 412 output from the baseline thermosphere model driven by measured geophysical indices
 413 (TIEGCM-GPI, grey curves) $F_{10.7}$ and K_p . The data assimilation IDEA output is given along
 414 each of the CubeSat orbits by the black curves.

$$415 \quad \sigma(m/o) = \sqrt{\frac{1}{N} \sum_{i=1}^N \left(\ln \frac{\rho_{m,i}}{\rho_{o,i}} - \ln \mu(m/o) \right)^2} \quad (5)$$

$$416 \quad RMSe(m/o) = \sqrt{\frac{1}{N} \sum_{i=1}^N \left(\ln \frac{\rho_{m,i}}{\rho_{o,i}} \right)^2} \quad (6)$$

417 As mentioned in Sutton (2018), these metrics have several properties that are desirable
 418 when working with the ratio of a quantity, such as neutral density, that varies exponentially. The
 419 $RMSe(m/o)$ and $\sigma(m/o)$ quantities are best interpreted as a percentage in the following way:
 420 $\% = 100 \times (\exp \sigma(m/o) - 1)$. The $RMSe(m/o)$ is a combination of $\mu(m/o)$ and $\sigma(m/o)$, as
 421 can be seen through the following relation: $RMSe(m/o)^2 = (\ln \mu(m/o))^2 + \sigma(m/o)^2$. The
 422 $RMSe(m/o)$ is therefore a good indicator of total model errors. However, if the intent is to drive
 423 a POD process using the density model, it may be more informative to use the $\sigma(m/o)$ metric,
 424 since a ballistic coefficient is typically estimated per satellite. In practice, this estimated ballistic
 425 coefficient will soak up errors not only in the assumed coefficient of drag, but also in the mean
 426 bias of the density model. Table 2 shows the overall performance of the three models, TIEGCM-
 427 GPI, HASDM, and IDEA at recreating the Spire CubeSat data.

428 During the period of interest, the IDEA method clearly outperforms HASDM in all three
 429 metrics. This is true of both the prior and posterior IDEA estimates of density; the former is a 6-
 430 hour persistence forecast of the external drivers while the latter is the fully assimilated solution.
 431 It should be noted, however, that IDEA has a clear advantage over the other two models in this
 432 comparison, since IDEA assimilates the very data that it is now being validated against. This
 433 scenario is somewhat unavoidable, as there is currently a lack of independent validation data
 434 sources related to neutral density. Because of this situation, any systematic errors in our data
 435 processing or underlying assumptions are not expected to be revealed by this comparison and
 436 validation. Instead, our findings are that the IDEA technique, as an estimation filter, has the
 437 requisite control authority to sufficiently adjust the model to the assimilated data set.

438 **Table 2.** Performance metrics of each model with respect to the assimilated Spire Global
 439 CubeSat data, calculated over the entire interval spanning days 266–343, 2018.

	TIEGCM-GPI	HASDM	IDEA	
			Prior	Posterior
$\mu(m/o)$	1.37	1.14	1.06	1.06
$\sigma(m/o)$	58.6%	51.7%	38.5%	33.9%
$RMSe(m/o)$	75.1%	55.0%	39.3%	34.7%

440 5 Summary and Conclusions

441 The increasing crowdedness of the satellite and debris populations in LEO necessitates
 442 improvements in how we detect, track, and catalog orbiting objects. Additionally, if we are to
 443 avoid catastrophic collisions in LEO, we must also be able to reliably predict the trajectories of
 444 satellites multiple days in advance. With the variability of the space environment, particularly
 445 thermospheric mass density, being the largest uncertainty in the orbit prediction chain, this study
 446 investigates new ways to monitor the upper atmosphere. In this notoriously data-starved region,
 447 the instrumentation commonly carried on recently launched LEO SmallSats and CubeSats,
 448 particularly GNSS receivers, can provide essential corrections to physics-based models of the
 449 thermosphere. Notably, the amount of data available from this new category of observation
 450 should continue to scale with the crowdedness of LEO, whereas the current ground-based
 451 tracking database remains limited in quantity and resolution.

452 In the current work, we have applied a post-processing method to the timeseries of POD
 453 ephemeris from three CubeSats in Spire’s constellation. This has allowed us to track the time
 454 evolution of orbital energy of each CubeSat over an orbit arc. Further application of a satellite-
 455 surface force model converts this information into a timeseries of *in situ* atmospheric mass
 456 density. By analyzing 78 days’ worth of data from late 2018, we were able to observe the impact
 457 of minor and moderate fluctuations in geomagnetic activity during the prevailing solar minimum
 458 conditions. We also found good agreement with HASDM, one of the only sources of
 459 thermospheric data currently available for comparison. While the resulting timeseries from a
 460 single satellite may be prone to errors, identified here simply as a discrepancy between density
 461 timeseries derived from co-orbiting CubeSats, this can be mitigated by assimilating timeseries
 462 from multiple data sets into a physics-based model of the thermosphere.

463 Additionally, with more advanced processing methods, it may be possible to lower the
464 noise for timeseries of individual CubeSats. The POD solutions used here were not specifically
465 tailored to the application of measuring density. One potential complication is that overfitting of
466 parameters or insufficient arc size may have led to significant noise in the inferred densities.
467 Future work will focus on improving the POD solutions to reduce noise and finding the optimal
468 size of the POD fitting window as a function of altitude, phase of the solar cycle, satellite
469 geometry characteristics, and GNSS instrument precision and errors. With these improvements
470 in place, it may even be possible to attain higher cadences than a single data point per orbit. This
471 has been demonstrated when using a state-of-the-art geodetic GNSS receiver (van den IJssel &
472 Visser, 2007), but extending this technique to GNSS-equipped constellations would provide
473 much needed global coverage of thermospheric observations. When paired with a suitable
474 assimilative, physics-based models of the thermosphere, there is great potential to lower the
475 uncertainty of orbit predictions across the LEO catalog, improve the accuracy of conjunction
476 assessments, and increase the efficacy of Space Traffic Management (STM) activities.

477 **Acknowledgments**

478 EKS, JPT, and TEB acknowledge the generous support of the University of Colorado at
479 Boulder Grand Challenge Grant: Space Weather Technology, Research, and Education Center
480 (SWx TREC). EKS gratefully acknowledges support from the NASA Operations-to-Research
481 (O2R) program under grant number 80NSSC20K1399. Support for SMM has been provided by
482 the National Defense Science and Engineering Graduate (NDSEG) Fellowship program. Data
483 from the Spire constellation used in this study may be requested and downloaded from the
484 NASA Commercial SmallSat Data Acquisition Program (CSDAP) website at
485 <https://earthdata.nasa.gov/esds/csdap>. The TIEGCM is developed and maintained by the National
486 Center for Atmospheric Research's High Altitude Observatory (HAO) and is available at
487 <https://www.hao.ucar.edu/modeling/tgcm/tie.php>.

488 **References**

- 489 Berger, T. E., Holzinger, M. J., Sutton, E. K., & Thayer, J. P. (2020). Flying Through
490 Uncertainty. *Space Weather*, *18*(1), 1–5. <https://doi.org/10.1029/2019SW002373>
- 491 Brandt, D. A., Bussy-Virat, C. D., & Ridley, A. J. (2020). A Simple Method for Correcting

- 492 Empirical Model Densities During Geomagnetic Storms Using Satellite Orbit Data. *Space*
493 *Weather*, 18(12). <https://doi.org/10.1029/2020SW002565>
- 494 Bruinsma, S., Fedrizzi, M., Yue, J., Siemes, C., & Lemmens, S. (2021). Charting Satellite
495 Courses in a Crowded Thermosphere. *Eos*, 102. <https://doi.org/10.1029/2021EO153475>
- 496 Codrescu, M. V., Fuller-Rowell, T. J., & Minter, C. F. (2004). An ensemble-type Kalman filter
497 for neutral thermospheric composition during geomagnetic storms. *Space Weather*, 2(11).
498 <https://doi.org/10.1029/2004SW000088>
- 499 Codrescu, M. V., Codrescu, S. M., & Fedrizzi, M. (2021). Storm Time Data Assimilation in the
500 Thermosphere Ionosphere with TIDA. *Submitted to Space Weather*.
501 <https://doi.org/10.1002/essoar.10505945.1>
- 502 Codrescu, S. M., Codrescu, M. V., & Fedrizzi, M. (2018). An Ensemble Kalman Filter for the
503 Thermosphere-Ionosphere. *Space Weather*, 16(1), 57–68.
504 <https://doi.org/10.1002/2017SW001752>
- 505 Fuller-Rowell, T. J., Minter, C. F., & Codrescu, M. V. (2004). Data assimilation for neutral
506 thermospheric species during geomagnetic storms. *Radio Science*, 39(1).
507 <https://doi.org/10.1029/2002RS002835>
- 508 Godinez, H. C., Lawrence, E., Higdon, D., Ridley, A., Koller, J., & Klimenko, A. (2015).
509 Specification of the Ionosphere-Thermosphere Using the Ensemble Kalman Filter (pp. 274–
510 283). https://doi.org/10.1007/978-3-319-25138-7_25
- 511 Hedin, A. E. (1991). Extension of the MSIS Thermosphere Model into the middle and lower
512 atmosphere. *Journal of Geophysical Research: Space Physics*, 96(A2), 1159–1172.
513 <https://doi.org/10.1029/90JA02125>
- 514 van den IJssel, J., & Visser, P. (2007). Performance of GPS-based accelerometry: CHAMP and
515 GRACE. *Advances in Space Research*, 39(10), 1597–1603.
516 <https://doi.org/10.1016/j.asr.2006.12.027>
- 517 Krauss, S., Temmer, M., Veronig, A., Baur, O., & Lammer, H. (2015). Thermospheric and
518 geomagnetic responses to interplanetary coronal mass ejections observed by ACE and
519 GRACE: Statistical results. *Journal of Geophysical Research: Space Physics*, 120(10),
520 8848–8860. <https://doi.org/10.1002/2015JA021702>

- 521 Matsuo, T., Fedrizzi, M., Fuller-Rowell, T. J., & Codrescu, M. V. (2012). Data assimilation of
522 thermospheric mass density. *Space Weather*, *10*(5). <https://doi.org/10.1029/2012SW000773>
- 523 Matsuo, T., Lee, I.-T., & Anderson, J. L. (2013). Thermospheric mass density specification using
524 an ensemble Kalman filter. *Journal of Geophysical Research: Space Physics*, *118*(3), 1339–
525 1350. <https://doi.org/10.1002/jgra.50162>
- 526 Minter, C. F., Fuller-Rowell, T. J., & Codrescu, M. V. (2004). Estimating the state of the
527 thermospheric composition using Kalman filtering. *Space Weather*, *2*(4).
528 <https://doi.org/10.1029/2003SW000006>
- 529 Morozov, A. V., Ridley, A. J., Bernstein, D. S., Collins, N., Hoar, T. J., & Anderson, J. L.
530 (2013). Data assimilation and driver estimation for the Global Ionosphere–Thermosphere
531 Model using the Ensemble Adjustment Kalman Filter. *Journal of Atmospheric and Solar-*
532 *Terrestrial Physics*, *104*, 126–136. <https://doi.org/10.1016/j.jastp.2013.08.016>
- 533 Murray, S. A., Henley, E. M., Jackson, D. R., & Bruinsma, S. L. (2015). Assessing the
534 performance of thermospheric modeling with data assimilation throughout solar cycles 23
535 and 24. *Space Weather*, *13*(4), 220–232. <https://doi.org/10.1002/2015SW001163>
- 536 Picone, J. M. (2005). Thermospheric densities derived from spacecraft orbits: Accurate
537 processing of two-line element sets. *Journal of Geophysical Research*, *110*(A3), A03301.
538 <https://doi.org/10.1029/2004JA010585>
- 539 Qian, L., Burns, A. G., Emery, B. A., Foster, B., Lu, G., Maute, A., et al. (2014). The NCAR
540 TIE-GCM: A Community Model of the Coupled Thermosphere/Ionosphere System. In
541 *Modeling the Ionosphere-Thermosphere System* (Vol. 9780875904, pp. 73–83).
542 <https://doi.org/10.1002/9781118704417.ch7>
- 543 Reigber, C., Schwintzer, P., Neumayer, K.-H., Barthelmes, F., König, R., Förste, C., et al.
544 (2003). The CHAMP-only earth gravity field model EIGEN-2. *Advances in Space*
545 *Research*, *31*(8), 1883–1888. [https://doi.org/10.1016/S0273-1177\(03\)00162-5](https://doi.org/10.1016/S0273-1177(03)00162-5)
- 546 Richmond, A. D., Ridley, E. C., & Roble, R. G. (1992). A thermosphere/ionosphere general
547 circulation model with coupled electrodynamics. *Geophysical Research Letters*, *19*(6), 601–
548 604. <https://doi.org/10.1029/92GL00401>
- 549 Storz, M. F., Bowman, B. R., Branson, M. J. I., Casali, S. J., & Tobiska, W. K. (2005). High

- 550 accuracy satellite drag model (HASDM). *Advances in Space Research*, 36(12), 2497–2505.
551 <https://doi.org/10.1016/j.asr.2004.02.020>
- 552 Sutton, E. K. (2009). Normalized Force Coefficients for Satellites with Elongated Shapes.
553 *Journal of Spacecraft and Rockets*, 46(1), 112–116. <https://doi.org/10.2514/1.40940>
- 554 Sutton, E. K. (2018). A New Method of Physics-Based Data Assimilation for the Quiet and
555 Disturbed Thermosphere. *Space Weather*, 16(6), 736–753.
556 <https://doi.org/10.1002/2017SW001785>
- 557 Sutton, E. K., Forbes, J. M., & Nerem, R. S. (2005). Global thermospheric neutral density and
558 wind response to the severe 2003 geomagnetic storms from CHAMP accelerometer data.
559 *Journal of Geophysical Research: Space Physics*, 110(A9).
560 <https://doi.org/10.1029/2004JA010985>
- 561 Sutton, E. K., Thayer, J. P., Wang, W., Solomon, S. C., Liu, X., & Foster, B. T. (2015). A self-
562 consistent model of helium in the thermosphere. *Journal of Geophysical Research: Space*
563 *Physics*, 120(8), 6884–6900. <https://doi.org/10.1002/2015JA021223>